High-fidelity Autonomous Navigation Based On DRO-LEO Inter-satellite Links

Li Shuanglin [1], Pu Jinghui [2] , Gao Yang [3], Wang Wenbin [4], Zhang Wei[5]

[1] *University of Chinese Academy of Sciences, No.19(A) Yuquan Road, Shijingshan District, Beijing 100049, China, 18009077498, lishuanglin20@mails.ucas.ac.cn*

[2] *University of Chinese Academy of Sciences, No.19(A) Yuquan Road, Shijingshan District, Beijing 100049, China, 15760594201, pujinghui20@mails.ucas.ac.cn*

[3] *Technology and Engineering Center for Space Utilization, Chinese Academy of Sciences, No. 9 Dengzhuang South Road, Haidian District, Beijing 100094, China, 15810131931, gaoyang@csu.ac.cn*

[4] *Technology and Engineering Center for Space Utilization, Chinese Academy of Sciences, No. 9 Dengzhuang South Road, Haidian District, Beijing 100094, China, 13581652038, wangwenbin@csu.ac.cn*

[5] *Technology and Engineering Center for Space Utilization, Chinese Academy of Sciences, No. 9 Dengzhuang South Road, Haidian District, Beijing 100094, China, 13693510178, zhangwei@csu.ac.cn*

Abstract: Distant retrograde orbits (DROs) are a family of stable orbits around the Moon that can even be maintained for hundreds of years while operating in the asymmetric gravitational field of Earth-Moon three-body space. The Cislunar DRO Exploration (CDROE) mission is supported by the Strategic Priority Research Program of the Chinese Academy of Sciences, which will launch three satellites into cislunar space, two of them, one into Distant Retrograde Orbit (DRO) and the other one into Low Earth Orbit (LEO). One of the mission objectives is to demonstrate the autonomous navigation performance based on LEO-DRO satellite-to-satellite tracking (SST) without relying on ground-based tracking. The asymmetric gravitational field makes the autonomous navigation of the DRO satellite possible when it establishes inter-satellite links with the LEO satellite, a technology known as Linked Autonomous Interplanetary Satellite Orbit Navigation (LiAISON). Given the shorter orbital period (about an hour and a half) of LEO, Rapidly-changing SST geometry will speed up the convergence time of autonomous navigation.
This paper mainly evaluates the autonomous navigation performance of DRO-LEO using realistic K-band radiometric link specifications. A high-fidelity measurement model, timing model, and orbital dynamical model are established to analyze what factors influence orbit determination and time synchronization, such as measurement frequency, integrator step, dynamics error, and measurement strategy. These research results will provide an important reference for engineering works.

Keywords: *DOWR, Autonomous Navigation, LiAISON, SST, Distant Retrograde Orbits (DROs).*

1. Introduction

The DROs are a type of three-body dynamic orbit that rotates the moon and earth. They are located at a highly asymmetrical gravitational field in cislunar space, which are hubs connecting low earth orbit, low moon orbit, and deep space. DROs have a series of unique dynamic characteristics, including long-term stability, and low fuel cost [1],[2], the propellant fuel cost for launching a spacecraft from our land launch site into DRO is lower than GEO, and Cislunar space accessibility. However, these characters haven't been used yet. In 2022, NASA went on

the Cislunar Autonomous Positioning System Technology Operations and Navigation Experiment (CAPSTONE) mission, which aimed at verifying the theory of the Linked Autonomous Interplanetary Satellite Orbit Navigation (LiAISON) in the Near Rectilinear Halo Orbit (NRHO) [3]. Similarly, the Chinese Academy of Sciences plans to launch a DRO orbiter in 2023. The Strategic Priority Research Program of the Chinese Academy of Sciences puts forward the CDROE mission, which plans to launch three satellites to build a large-scale experimental constellation to take advantage of DRO's unique properties. In the CDROE mission, experiments such as space-based autonomous orbit determination based on SST range measurements and autonomous maneuvering cruise of cislunar spacecraft can be supportive for establishing space-based stations and manned space stations in cislunar space. SST range measurements and autonomous navigation are parts of the key research contents. Autonomous navigation is based on inter-satellite measurement, which means that satellites can get their orbit states and clocks by using SST range measurements without the participation of ground stations, and it will be supported by the LiAISON technique which has been verified in literature [4].

To improve the observability of autonomous navigation, CDROE takes full use of the asymmetry of the gravitational field in the cislunar space and chooses the appropriate orbit according to the specific gravitational field distribution of the cislunar space, so the 2:1 resonant DRO orbit is chosen, the trajectory of DRO is shown in Fig. 1. The subgraph (a) and (b) show the trajectory expressed in J2000 coordinate system and the Earth-Moon rotating coordinate system.

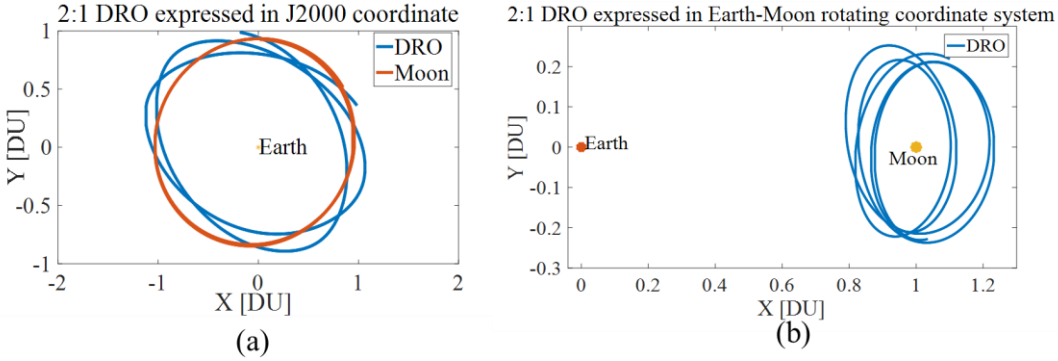

Figure 1. trajectory of DRO.

Due to the short orbital period of the LEO, the SST range of the link established between the DRO and the LEO changes rapidly, and the measurement construction is good. The navigation scenario proposed in the mission is shown in Fig. 2.

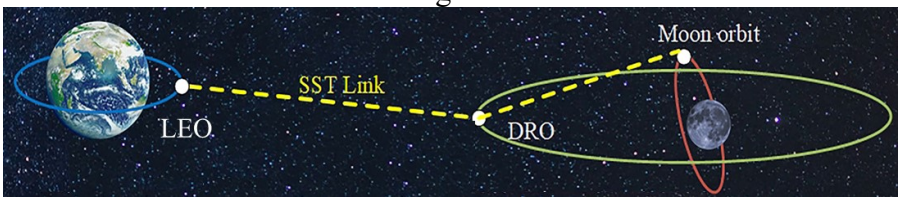

Figure 2. SST links between a DRO and a LEO.

In this paper, attention is paid to researching the navigation performance of the DRO-LEO link on high-fidelity measurement simulations. To elaborate, this paper introduces the payloads on the satellites and three kinds of measurement modes firstly. Secondly, this paper establishes a high-fidelity measurement model considering signal transmission time, equipment delays, onboard clock deterministic and stochastic errors, and measurement white noise. However, the relativity influence and signal path delay haven't been considered yet. Thirdly, the measurement model and orbit determination method are proposed. Next, this paper introduces the orbit setting

and then researches navigation performance which is influenced by various factors, such as integrator, the integration step, navigation dynamic model, and the measurement type. Results show that the DOWR system can improve navigation performance by decoupling the orbit states and clock information, and satellites can get high-precision navigation results by establishing an appropriate dynamical integration model and observation model. And navigation performance is closely related to the accuracy of a dynamic model, and the measurement mode greatly influences the convergence speed.

2. Payloads Configuration And Measurement Mode

2.1 Payloads Configuration

In this mission, each satellite will carry a hardware platform, a transceiver system of K-Band, and an onboard clock. The transceiver system of the K-Band is used for inter-satellite communication and measurement, which can be supportive for autonomous navigation. And the set of EIRP, the value of G/T, and other parameters are shown in Tab. 1

Table 1. K-band measurement payload

Platform	Antenna aperture (m)	Frequency transmission (GHz)	Frequency reception (GHz)	EIRP (dBW)	G/T (dBK)
DRO satellite	0.22	26.5	23	40.4	1.61
LEO satellite	0.6	23	26.5	50	11.2

According to the existing literature [5], the free space propagation loss can be calculated. And then thermal noise can be calculated by carrier-to-noise ratio and signal receive power. The diagram of system thermal noise versus inter-range between LEO and DRO is illustrated in Fig. 3, which shows that the thermal noise is less than 0.1m.

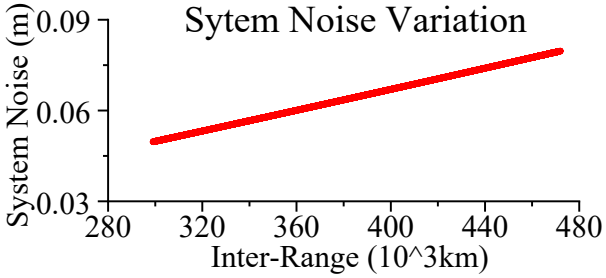

Figure 3. Relation between the SST range and system thermal noise.

Another correlating payload is a small Rubidium clock onboard DRO, it ensures high-quality operation of communication and measurement by providing an accurate time system. The clock model includes deterministic and stochastic errors, the deterministic clock errors are usually modeled as a polynomial series form of second order. The specification of a small rubidium clock is described in Tab. 2. The LEO is equipped with a high stability crystal oscillator and a GNSS receiver, which can facilitate obtaining its precise time system and states. The timing result fits zero mean normal distribution with the standard deviation of 20ns (1σ).

Table 2. Major specification of rubidium clock

Specification item	Value
Output frequency	10MHz
Frequency accuracy (A1)	$\leq \pm 5\times10^{-9}$
Frequency drifting rate (A2)	$\leq 5\times10^{-12}$/d

Frequency stability	1s	$\leq 3\times10^{-11}$
	10s	$\leq 1\times10^{-11}$
	100s	$\leq 3\times10^{-12}$
	1000s	$\leq 1\times10^{-12}$
	10000s	$\leq 3\times10^{-13}$

2.2. CROSSLINK MEASUREMENTS

Different measurement types are designed to evaluate navigation performance, the main three measurement types are introduced as follows:

(1) Dual One-Way Ranging System

A DOWR system combines the one-way range measurements from two satellites at the same receiving epoch. The sum combination almost eliminates clock error, and the subtractive combination almost eliminates geometric range. Thereby clock information is decoupled from geometry-ranging information, so convergence speed and accuracy of navigation can be improved during the orbit determination procedure. In this measurement mode, the influence of different integrators, integration steps, and dynamic models will be further evaluated. In this measurement mode, both LEO and DRO receive signals for 1h/12h.

(2) One-Way Ranging System

The one-way ranging system is the most traditional measurement type, which was widely used and studied already. In this measurement mode, LEO receives signals 1h/12h.

(3) DOWR + One-Way.

We test the combination of DOWR and one-way measurement, to decrease the power consumption of the K-band payload. Compared to the DOWR system, resources are largely reserved. And when compared with a one-way ranging system, this measurement type can get good use of the DOWR system to get clock parameters converging quickly. In this measurement mode, the frequency of one-way ranging measurement is 1h/12h and the frequency of DOWR is 1h/120h.

3. Dual One-Way Ranging Measurement Model

The one-way ranging system is a simplified version of the DOWR system, so attention is paid to establishing a DOWR measurement model.

3.1. Clock Model

The clock model includes deterministic and stochastic errors. It is assumed that the clock onboard DRO is a Rubidium clock, and deterministic clock errors are usually modeled as a polynomial series form of second order. So, the clock model of DRO can be expressed as follows:

$$\begin{aligned}
&\delta\tau_{\mathrm{D}}(t_{\mathrm{D}}) = \mathrm{A}_0^{\mathrm{D}}(t_0) + \mathrm{A}_1^{\mathrm{D}}(t_{\mathrm{D}} - t_0) + 0.5 \times \mathrm{A}_2^{\mathrm{D}}(t_{\mathrm{D}} - t_0)^2 + \zeta_{\mathrm{D}}(t_{\mathrm{D}}) \\
&\dot{\delta}\tau_{\mathrm{D}}(t_{\mathrm{D}}) = \mathrm{A}_1^{\mathrm{D}} + \mathrm{A}_2^{\mathrm{D}}(t_{\mathrm{D}} - t_0) \\
&\ddot{\delta}\tau_{\mathrm{D}}(t_{\mathrm{D}}) = \mathrm{A}_2^{\mathrm{D}}
\end{aligned} \tag{1}$$

Where, the t_0 denotes reference time, and t_{D} denotes current time. And $t_{\mathrm{D}} - t_0$ is controlled in 1 day to ensure the accuracy of clock modeling. $\mathrm{A}_0^{\mathrm{D}}$ denotes the clock offset, the $\mathrm{A}_1^{\mathrm{D}}$ denotes clock drift and the $\mathrm{A}_2^{\mathrm{D}}$ denotes the clock frequency drift. $\zeta_{\mathrm{D}}(t_{\mathrm{D}})$ denotes the stochastic clock noise.
In our research, the LEO is equipped with a crystal oscillator with high stability, and the LEO can receive a GNSS navigation signal. Based on the clock discipline system, the timing result can be seen as random, and the timing accuracy is 20 ns(1σ).

3.2. Ranging Model

The schematic diagram of the DOWR measurement is as follows: Pseudorange measurement model of Satellite D (refers to DRO) and satellite L (refers to LEO) receive signals from each other can be expressed as follows:

$$\begin{aligned}
R_{\mathrm{D}}^{\mathrm{L}}\left(t_{\mathrm{D}}\right) &= \left\| \boldsymbol{r}_{\mathrm{D}}\left(t_{\mathrm{D}}\right) - \boldsymbol{r}_{\mathrm{Y}}\left(\tilde{t}_{\mathrm{D}}\right) \right\| + c \cdot \left(D_{\mathrm{D}}^{\mathrm{R}} + D_{\mathrm{L}}^{\mathrm{S}}\right) + c \cdot \left(\delta\tau_{\mathrm{D}}(t_{\mathrm{D}}) - \delta\tau_{\mathrm{L}}(\tilde{t}_{\mathrm{D}})\right) + \varepsilon_{\mathrm{D}} \\
R_{\mathrm{L}}^{\mathrm{D}}\left(t_{\mathrm{L}}\right) &= \left\| \boldsymbol{r}_{\mathrm{L}}\left(t_{\mathrm{L}}\right) - \boldsymbol{r}_{\mathrm{D}}\left(\tilde{t}_{\mathrm{L}}\right) \right\| + c \cdot \left(D_{\mathrm{L}}^{\mathrm{R}} + D_{\mathrm{D}}^{\mathrm{S}}\right) + c \cdot \left(\delta\tau_{\mathrm{L}}(t_{\mathrm{L}}) - \delta\tau_{\mathrm{D}}(\tilde{t}_{\mathrm{L}})\right) + \varepsilon_{\mathrm{L}}
\end{aligned} \tag{2}$$

Where t_{D} denotes the time of DRO receiving signals from LEO at $\tilde{t}_{\mathrm{D}}$, and t_{L} denotes the time of LEO receiving signals from DRO at $\tilde{t}_{\mathrm{L}}$. In this paper, LEO and DRO receive the signal at the same time, $t_{\mathrm{D}} = t_{\mathrm{L}}$. $R_{\mathrm{D}}^{\mathrm{L}}$ and $R_{\mathrm{L}}^{\mathrm{D}}$ denote the pseudorange measurement data received by DRO and LEO. $\boldsymbol{r}_{\mathrm{D}}, \boldsymbol{r}_{L}$ denote the position of DRO and LEO. $D_{\mathrm{D}}^{\mathrm{R}}$, $D_{\mathrm{L}}^{\mathrm{S}}$, $D_{\mathrm{L}}^{\mathrm{R}}$, $D_{\mathrm{D}}^{\mathrm{S}}$ denote equipment delays. $\delta\tau_{\mathrm{D}}, \delta\tau_{\mathrm{L}}$ denote the clock of DRO and LEO. Thermal noise ε_{D}, ε_{L} are modeled as White Gaussian Noise, $\varepsilon \sim N(0, \sigma_{\varepsilon})$. In K-band ranging, the thermal noise of the system (1σ) is less than 0.5 m, which is analyzed in Chap.2.

3.3. Measurement linear combination

The sum combination and subtraction combination of DOWR pseudo-range measurement are expressed as follows:

1) **The sum combination of DOWR pseudorange measurement** is summed $R_{\mathrm{D}}^{\mathrm{L}}\left(t_{\mathrm{D}}\right)$ and $R_{\mathrm{L}}^{\mathrm{D}}\left(t_{\mathrm{D}}\right)$, and then divided by 2, which can be expressed as follows:

$$z_{\mathrm{com}}(t_i) = \frac{R_{\mathrm{D}}^{\mathrm{L}}(t_{\mathrm{D}}) + R_{\mathrm{L}}^{\mathrm{D}}(t_{\mathrm{L}})}{2} = \frac{1}{2} \cdot \left[\rho_{\mathrm{D}}^{\mathrm{L}} + \rho_{\mathrm{L}}^{\mathrm{D}} + c \cdot D_{\mathrm{com}} + c \cdot \left((t_{\mathrm{D}} - \tilde{t}_{\mathrm{L}}) \dot{\delta}\tau_{\mathrm{D}} \right) + c \cdot \Delta\delta\tau_{\mathrm{L}} + \varepsilon_{\mathrm{D}} + \varepsilon_{\mathrm{L}} \right] \tag{3}$$

Where the $D_{\mathrm{com}} = c \cdot \left(D_{\mathrm{D}}^{\mathrm{R}} + D_{\mathrm{L}}^{\mathrm{S}} + D_{\mathrm{D}}^{\mathrm{S}} + D_{\mathrm{L}}^{\mathrm{R}} \right)$ denotes the influence of equipment delays in the sum combination. $\Delta\delta\tau_{\mathrm{L}}$ represent the variation of the timing clock offset in the time span $t_{\mathrm{L}} - \tilde{t}_{\mathrm{D}}$. The

variation of the Rubidium clock's frequency presents the characteristic of white noise, and the stochastic clock noise after integration belongs to the random walk model, which has a time-correlated characteristic, the value of stochastic clock noise is not very big. Because the stochastic clock noise is continuous and ε_{D}, ε_{L} can be nearly canceled out with opposite signs in the sum combination, the influence can be eliminated.

It is easy to find that the sum combination can eliminate the fixed difference in clock offset and stochastic errors. The remaining elements include the sum of geometric distances in different directions, the clock drift when a signal transmitting from one satellite to another, and thermal noise in the measurement. The clock frequency drift $\mathrm{A}_2^{\mathrm{D}}$ of the Rubidium clock onboard DRO is about 3E-13/day, the affection can be ignored. When it comes to the Hydrogen maser, the clock frequency drift is smaller, the accuracy is about 5E-15/day. The clock offset from GNSS is continuous, not completely discrete and random, so in a few seconds, the value $\Delta\delta\tau_{\mathrm{L}}$ is at the nanometer level. The equipment delay has a relationship with the satellite's temperature change, and the temperature changes slowly in a short period, equipment delays can be modeled as a constant. In the orbit determination process, equipment delays can be estimated to reduce their influence.

2) **The subtraction combination of DOWR pseudo-range measurement** is subtracting $R_{\mathrm{D}}^{\mathrm{L}}\left(t_{\mathrm{D}}\right)$ from $R_{\mathrm{L}}^{\mathrm{D}}\left(t_{\mathrm{D}}\right)$, and then dividing by 2, which can be expressed as follows:

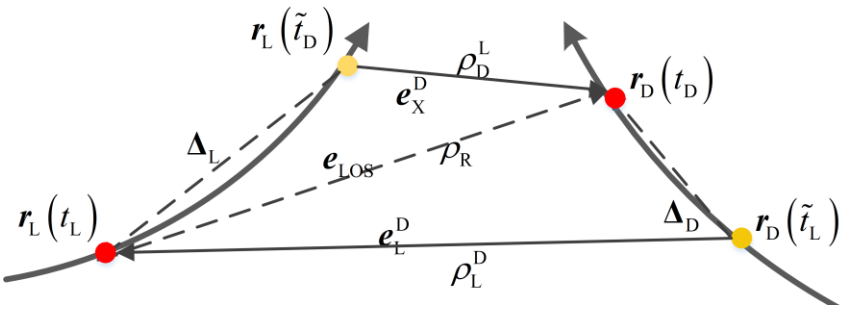

Figure 4. Schematic diagram of signal transmission in the DOWR system

Firstly, the instantaneous distance of the measurement model needs to be corrected, because the two satellites have relative motion, and the geometric distances in different directions are not equal and cannot be directly eliminated. The schematic diagram of signal transmission can be shown in Fig. 4. In Fig. 4, $\rho_{\mathrm{R}}=\left\|\boldsymbol{r}_{\mathrm{D}}\left(t_{\mathrm{D}}\right)-\boldsymbol{r}_{\mathrm{L}}\left(t_{\mathrm{L}}\right)\right\|$ represents the instantaneous inter-satellite geometric distance of two satellites at the receiving time, the signal transmission geometric distance $\rho_{\mathrm{D}}^{\mathrm{L}}=\left\|\boldsymbol{r}_{\mathrm{D}}\left(t_{\mathrm{D}}\right)-\boldsymbol{r}_{\mathrm{L}}\left(\tilde{t}_{\mathrm{D}}\right)\right\|$ $\rho_{\mathrm{L}}^{\mathrm{D}}=\left\|\boldsymbol{r}_{\mathrm{L}}\left(t_{\mathrm{L}}\right)-\boldsymbol{r}_{\mathrm{D}}\left(\tilde{t}_{\mathrm{L}}\right)\right\|$ need to be corrected to it. $\boldsymbol{\Delta}_{\mathrm{D}}$ ($\boldsymbol{\Delta}_{\mathrm{D}}=\boldsymbol{r}_{\mathrm{D}}(t_{\mathrm{D}})-\boldsymbol{r}_{\mathrm{D}}(\tilde{t}_{\mathrm{L}})$)and $\boldsymbol{\Delta}_{\mathrm{L}}$ ($\boldsymbol{\Delta}_{\mathrm{L}}=\boldsymbol{r}_{\mathrm{L}}(t_{\mathrm{L}})-\boldsymbol{r}_{\mathrm{L}}(\tilde{t}_{\mathrm{D}})$) are displacement vectors, that represent the displacement variation of two satellites during signal transmission time.

The correction of the signal transmission geometric distance $\rho_{\mathrm{D}}^{\mathrm{L}}$ and $\rho_{\mathrm{L}}^{\mathrm{D}}$ to the instantaneous distance ρ_{R} is performed as follows:

$$\begin{aligned}\rho_{\mathrm{D}}^{\mathrm{L}} &\approx \rho_{\mathrm{R}} + \boldsymbol{\Delta}_{\mathrm{L}}\boldsymbol{e}_{\mathrm{LOS}} \\ \rho_{\mathrm{L}}^{\mathrm{D}} &\approx \rho_{\mathrm{R}} - \boldsymbol{\Delta}_{\mathrm{D}}\boldsymbol{e}_{\mathrm{LOS}}\end{aligned} \tag{4}$$

Where $\boldsymbol{e}_{\mathrm{LOS}}=\dfrac{\boldsymbol{r}_{\mathrm{D}}-\boldsymbol{r}_{\Delta_{\mathrm{D}}}}{\rho_{\mathrm{R}}}$ denotes the unit vector of the position of LEO pointing to DRO at the signal receiving time. Eq. (4) is to project the displacement vectors to the inter-satellite unit vector. The correction to instantaneous distance will bring errors to the model, which can be shown in Fig. 5. In Fig. 5 ε denotes the correction error. When the distance between two satellites is far, and the velocity vector is nearly perpendicular to the inter-satellite unit vector, the errors will be large. In the scenario of LEO-DRO, the SST range is about 400000 km, so the transmission time is about 1.5s. In the worst circumstance, LEO's motion direction is perpendicular to the inter-satellite unit vector, the maximum displacement is 10km, and the largest correction error is about 15cm. But in the most normal situation, the correction error is at the cm level.

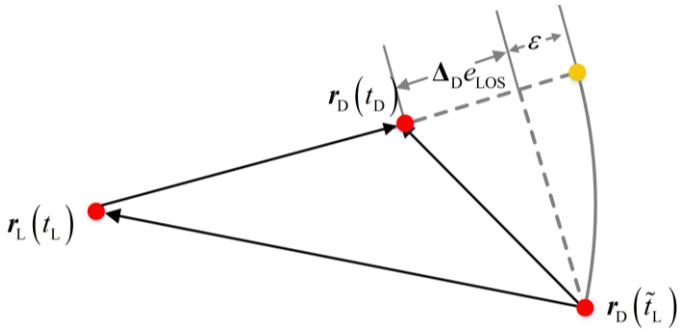

Figure 5. Schematic diagram of Instantaneous range correction in the DOWR system

Then, we subtract $R_{\mathrm{D}}^{\mathrm{L}}(t_{\mathrm{D}})$ from $R_{\mathrm{L}}^{\mathrm{D}}(t_{\mathrm{D}})$ and then divide it by 2.

$$\begin{aligned}z_{\mathrm{sub}} &= \frac{R_{\mathrm{D}}^{\mathrm{L}}(t_{\mathrm{D}})-R_{\mathrm{L}}^{\mathrm{D}}(t_{\mathrm{L}})}{2} \\ &\approx \frac{1}{2}\left[\left(\boldsymbol{\Delta}_{\mathrm{D}}+\boldsymbol{\Delta}_{\mathrm{L}}\right)\cdot\boldsymbol{e}_{\mathrm{LOS}}+c\cdot D_{\mathrm{sub}}+c\cdot\left(\delta\tau_{\mathrm{D}}(t_{\mathrm{D}})-\delta\tau_{\mathrm{L}}(\tilde{t}_{D})\right)-c\cdot\left(\delta\tau_{\mathrm{L}}(t_{\mathrm{L}})-\delta\tau_{\mathrm{D}}(\tilde{t}_{\mathrm{L}})\right)+\varepsilon_{\mathrm{D}}-\varepsilon_{\mathrm{L}}\right] \\ &\approx \frac{1}{2}\left[\left(\boldsymbol{\Delta}_{\mathrm{D}}+\boldsymbol{\Delta}_{\mathrm{L}}\right)\cdot\boldsymbol{e}_{\mathrm{LOS}}+c\cdot D_{\mathrm{sub}}+\varepsilon_{\mathrm{D}}-\varepsilon_{\mathrm{Y}}\right]+c\cdot(\mathrm{A}_0^{\mathrm{D}}-\delta\tau_{\mathrm{L}}) \\ &\quad +c\left(t_{\mathrm{D}}-t_0-\frac{\Delta t}{2}\right)\mathrm{A}_1^{\mathrm{D}}+\frac{c}{4}\left((t_{\mathrm{D}}-t_0)^2+(t_{\mathrm{D}}-t_0-\Delta t)^2\right)\mathrm{A}_2^{\mathrm{D}}+\zeta_{\mathrm{D}}(t_{\mathrm{D}})\end{aligned} \tag{5}$$

Where Δt denotes the average signal transmission time in the DOWR system, $\Delta t \doteq \dfrac{\Delta t_{\mathrm{D}}+\Delta t_{\mathrm{L}}}{2}$.

The signal transmission time is nearly equal, so we can have $t_{\mathrm{X}}-\tilde{t}_{\mathrm{Y}}\approx\Delta t$ and $t_{\mathrm{L}}-\tilde{t}_{\mathrm{D}}\approx\Delta t$. The $D_{\mathrm{sub}}\doteq D_{\mathrm{D}}^{\mathrm{R}}+D_{\mathrm{L}}^{\mathrm{S}}-D_{\mathrm{D}}^{\mathrm{S}}-D_{\mathrm{L}}^{\mathrm{R}}$ denotes the equipment delay term in the subtraction combination. And the clock onboard signal sending time is correct to the signal receiving time by using Taylor expansion to the Quadratic nonlinear item.

We can find that the subtraction combination can eliminate items of inter-satellite ranges, and remain the clock items. The clock offset between the clock onboard the DRO satellite and GNSS

timing is $A_0^D - \delta\tau_L$, and the equipment delay item is coupled with clock items and not distinguishable, so during the orbit determination process, we will estimate them as a variable parameter. The main errors come from the stochastic clock noise error of clock onboard DRO, GNSS clock offset of LEO, and measurement thermal noise.

3.4. Linearization of the measurement model

(1) the sum combination (for the distance part)

The linearization of geometric distance $\rho_D^L + \rho_L^D$, and can be performed at the known states $\boldsymbol{r}_{D0}(t_D), \boldsymbol{v}_{D0}(t_D)$ and $\boldsymbol{r}_{L0}(t_L), \boldsymbol{v}_{L0}(t_L)$ at the signal receiving time:

$$\begin{aligned}\rho &= \frac{1}{2}\left(\rho_D^L + \rho_L^D\right) = \frac{1}{2}\left(\left\|\boldsymbol{r}_D(t_D) - \boldsymbol{r}_L(\tilde{t}_D)\right\| + \left\|\boldsymbol{r}_L(t_L) - \boldsymbol{r}_D(\tilde{t}_L)\right\|\right) \\ &= \frac{1}{2}\left(\rho_0 + \frac{\partial h}{\partial \boldsymbol{r}_D}\Delta\boldsymbol{r}_D + \frac{\partial h}{\partial \boldsymbol{v}_D}\Delta\boldsymbol{v}_D + \frac{\partial h}{\partial \boldsymbol{r}_L}\Delta\boldsymbol{r}_L + \frac{\partial h}{\partial \boldsymbol{v}_L}\Delta\boldsymbol{v}_L\right)\end{aligned} \tag{6}$$

Where Δ represents the updated value of the estimated parameters, then we have $\Delta\boldsymbol{r} = \boldsymbol{r}(t) - \boldsymbol{r}_0(t)$, $\Delta\boldsymbol{v} = \boldsymbol{v}(t) - \boldsymbol{v}_0(t)$, and $\rho_0 = \left\|\boldsymbol{r}_{D0}(t_D) - \boldsymbol{r}_{L0}(\tilde{t}_D)\right\| + \left\|\boldsymbol{r}_{L0}(t_L) - \boldsymbol{r}_{D0}(\tilde{t}_L)\right\|$. The Partial derivatives are as follows:

$$\begin{aligned}\frac{\partial\rho}{\partial\boldsymbol{r}_D} &= \frac{1}{2}\left(\boldsymbol{e}_D^{LT} - \boldsymbol{e}_L^{DT}\cdot\boldsymbol{\Phi}_{rr}^D\right) \\ \frac{\partial\rho}{\partial\boldsymbol{v}_D} &= -\frac{1}{2}\left(\boldsymbol{e}_L^{DT}\cdot\boldsymbol{\Phi}_{rv}^D\right) \\ \frac{\partial\rho}{\partial\boldsymbol{r}_L} &= \frac{1}{2}\left(\boldsymbol{e}_L^{DT} - \boldsymbol{e}_D^L(t_i)^T\cdot\boldsymbol{\Phi}_{rr}^L\right) \\ \frac{\partial\rho}{\partial\boldsymbol{v}_L} &= -\frac{1}{2}\left(\boldsymbol{e}_D^{LT}\cdot\boldsymbol{\Phi}_{rv}^L\right)\end{aligned} \tag{7}$$

Where $\boldsymbol{e}_L^D = \frac{\boldsymbol{r}_L(t_L) - \boldsymbol{r}_D(\tilde{t}_L)}{\rho_L^D}$ and $\boldsymbol{e}_D^L = \frac{\boldsymbol{r}_D(t_D) - \boldsymbol{r}_L(\tilde{t}_D)}{\rho_1^2}$ are unit vectors, the state transition matrix is as follows:

$$\begin{aligned}\boldsymbol{\Phi}^D\left(\tilde{t}_D, t_D\right) &= \begin{pmatrix}\boldsymbol{\Phi}_{rr}^D & \boldsymbol{\Phi}_{rv}^D \\ \boldsymbol{\Phi}_{vr}^D & \boldsymbol{\Phi}_{vv}^D\end{pmatrix} \\ \boldsymbol{\Phi}^L\left(\tilde{t}_L, t_L\right) &= \begin{pmatrix}\boldsymbol{\Phi}_{rr}^L & \boldsymbol{\Phi}_{rv}^L \\ \boldsymbol{\Phi}_{vr}^L & \boldsymbol{\Phi}_{vv}^L\end{pmatrix}\end{aligned} \tag{8}$$

(2) the subtraction combination (for the clock part)

If one clock onboard the satellite of the inter-satellite link is known, the clock estimated parameters represent the absolute clock. As the clock onboard LEO can get absolute time by GNSS, so the estimated time parameters are as follow:

$$\begin{aligned}\delta \mathrm{A}_0 &= \mathrm{A}_0^{\mathrm{D}} - \delta t_2 + \frac{D_{\mathrm{sub}}}{2} \\ \delta \mathrm{A}_1 &= \mathrm{A}_1^{\mathrm{D}} \\ \delta \mathrm{A}_2 &= \mathrm{A}_2^{\mathrm{D}}\end{aligned} \tag{9}$$

And the partial derivatives with respect to clock parameters are as follow:

$$\begin{aligned}\frac{\partial z_{\mathrm{sub}}}{\partial (c\delta \mathrm{A}_0)} &= 1 \\ \frac{\partial z_{\mathrm{sub}}}{\partial (c\delta \mathrm{A}_1)} &= \frac{t_{\mathrm{D}} + t_{\mathrm{L}}}{2} - t_0 - \frac{\Delta t}{2} \\ \frac{\partial z_{\mathrm{sub}}}{\partial (c\delta \mathrm{A}_2)} &= \frac{1}{4}\left[(\frac{t_{\mathrm{D}} + t_{\mathrm{L}}}{2} - t_0)^2 + (\frac{t_{\mathrm{D}} + t_{\mathrm{L}}}{2} - t_0 - \Delta t)^2 \right]\end{aligned} \tag{10}$$

Where c denotes the speed of light, which is generally estimated by multiplying the clock difference parameter with the speed of light.

4. Navigation Method

Navigation starts with an initial state its uncertainty. After orbit propagation using the specified dynamic models, a reference trajectory is achieved. In fact, the reference trajectory is different from the true trajectory due to its initial state errors and dynamic model errors. The navigation must determine a new state estimation of the satellite based on a set of measurement data received by these satellites, matching the reference trajectory as closely as possible. Several algorithms are commonly used to process measurements and provide the best state estimate of satellites. The Extended Kalman Filter (EKF) [6] selected by this study is one type of fundamental sequential estimation method and it is suitable for the real-time navigation of satellites.

4.1 Estimated states

During the autonomous navigation process, the estimated parameters include the position vector $\boldsymbol{r}_D$, $\boldsymbol{r}_L$ and velocity vector $\boldsymbol{v}_D, \boldsymbol{v}_L$ of two satellites, the absolute clock parameters of the DRO satellite $c\delta \mathrm{A}_0, c\delta \mathrm{A}_1$ and $c\delta \mathrm{A}_2$, the dynamic parameters C_D, C_R and the equipment delay term $\frac{D_{\mathrm{com}}}{2}$. The $\boldsymbol{Y}$ denotes the position vector $\boldsymbol{r}_D$, $\boldsymbol{r}_L$ and velocity vector $\boldsymbol{v}_D, \boldsymbol{v}_L$ of two satellites, the $\boldsymbol{T}$ denotes the clock parameters and the $\boldsymbol{a}$ denotes the dynamic parameters. The $\boldsymbol{X}$ denotes all the estimated states, as follows:

$$
\begin{aligned}
\boldsymbol{Y} &= \begin{bmatrix} \boldsymbol{r}_D^{\mathrm{T}} & \boldsymbol{v}_D^{\mathrm{T}} & \boldsymbol{r}_L^{\mathrm{T}} & \boldsymbol{v}_L^{\mathrm{T}} \end{bmatrix} \\
\boldsymbol{T} &= \begin{bmatrix} c\mathrm{A}_0^{\mathrm{D}} & c\mathrm{A}_1^{\mathrm{D}} & c\mathrm{A}_2^{\mathrm{D}} \end{bmatrix}^{\mathrm{T}} \\
\boldsymbol{a} &= \begin{bmatrix} C_D & C_R \end{bmatrix} \\
\boldsymbol{X} &= \begin{bmatrix} \boldsymbol{Y} & \boldsymbol{T} & \boldsymbol{a} & \dfrac{D_{com}}{2} \end{bmatrix}
\end{aligned}
\tag{11}
$$

4.2 Time update

To compensate for the dynamic model errors, we add process noise $\boldsymbol{u}(t)$ into the dynamic model, the propagation of $\boldsymbol{Y}$ overtime is determined by numerical integration of a set of ordinary first-order differential equations as follows:

$$
\frac{d\boldsymbol{Y}(t)}{dt} = \boldsymbol{f}(\boldsymbol{Y},t) = \boldsymbol{f}(\boldsymbol{Y}(t),\boldsymbol{u}(t),t) \tag{12}
$$

Where process noise $\boldsymbol{u}(t)$ is a Gaussian white noise vector whose mean value is the zero vector. The state transition matrix $\boldsymbol{\Phi}_{\boldsymbol{Y}}(t,t_0)$ at an arbitrary time t with respect to the initial time t_0 can be computed in terms of the variational equation as follows:

$$
\frac{d}{dt}\boldsymbol{\Phi}_{\boldsymbol{Y}}(t,t_0) = \frac{\partial \boldsymbol{f}(\boldsymbol{Y}(t),\boldsymbol{u}(t),t)}{\partial \boldsymbol{Y}(t)}\boldsymbol{\Phi}_{\boldsymbol{Y}}(t,t_0) \tag{13}
$$

The process noise transform matrix is denoted by the following, and can be expanded as:

$$
\boldsymbol{\Gamma}_{\boldsymbol{Y}}(t,t_0) = \frac{\partial \boldsymbol{Y}(t)}{\partial \boldsymbol{u}(t_0)} = \begin{bmatrix} \Delta t^2/2 \times \boldsymbol{I}_{3\times 3} & & \\ \Delta t \times \boldsymbol{I}_{3\times 3} & & \\ & \Delta t^2/2 \times \boldsymbol{I}_{3\times 3} & \\ & \Delta t \times \boldsymbol{I}_{3\times 3} & \end{bmatrix} \tag{14}
$$

Where $\Delta t\left(=t_i - t_0\right)$ denotes the step size and $\boldsymbol{I}$ is the identity matrix.

Given the initial state $\boldsymbol{X}_0$ and state covariance $\boldsymbol{P}_0$ at the time t_0, the EKF processes SST range data at consecutive measurement epochs. This process comprises two steps. The first step is the "time update," where the state and covariance evolve from the previous time t_i to the current time t_{i+1}, which is given as follows:

$$
\begin{aligned}
\boldsymbol{X}_{i+1|i} &= \boldsymbol{X}\left(t_{i+1}, \boldsymbol{X}\left(t_i\right) = \boldsymbol{X}_i\right) + \boldsymbol{\Gamma}_{i+1|i}\boldsymbol{u}_i \\
\boldsymbol{P}_{i+1|i} &= \boldsymbol{\Phi}_{i+1|i}\boldsymbol{P}_i\boldsymbol{\Phi}_{i+1|i}^{\mathrm{T}} + \boldsymbol{\Gamma}_{i+1|i}\boldsymbol{Q}_c\boldsymbol{\Gamma}_{i+1|i}^{\mathrm{T}}
\end{aligned}
\tag{15}
$$

Where $\boldsymbol{Q}_c$ is a 6×6 state noise compensation matrix.

Propagation of the state and covariance includes numerical integration of the orbital dynamics and the variation equations. The clock parameters, dynamic parameters, and equipment delay term remain unchanged during the time update process.

Thus, the state transition matrix $\boldsymbol{\Phi}_{i+1|i}$ is expressed as follows:

$$\boldsymbol{\Phi}_{i+1|i}=\begin{pmatrix} \boldsymbol{\Phi}_{\boldsymbol{Y}}\left(t_{i+1},t_i\right) & \boldsymbol{0}_{12\times3} & \dfrac{\partial \boldsymbol{Y}\left(t_{i+1}\right)}{\partial \boldsymbol{a}\left(t_i\right)} & \boldsymbol{0}_{12\times1} \\ \boldsymbol{0}_{3\times12} & \boldsymbol{I}_{3\times3} & \boldsymbol{0}_{3\times2} & \boldsymbol{0}_{3\times1} \\ \boldsymbol{0}_{2\times12} & \boldsymbol{0}_{2\times3} & \boldsymbol{I}_{2\times2} & \boldsymbol{0}_{2\times1} \\ \boldsymbol{0}_{1\times12} & \boldsymbol{0}_{1\times3} & \boldsymbol{0}_{1\times2} & 1 \end{pmatrix} \tag{16}$$

Where $\boldsymbol{0}$ is the zero matrix. The process noise transform matrix $\boldsymbol{\Gamma}_{i+1|i}$ is computed by:

$$\boldsymbol{\Gamma}_{i+1|i}=\frac{\partial \boldsymbol{X}(t_i)}{\partial \boldsymbol{u}(t_{i-1})}=\begin{bmatrix} \boldsymbol{\Gamma}_{\boldsymbol{Y}}(t_{i+1},t_i) \\ \boldsymbol{0}_{6\times6} \end{bmatrix} \tag{17}$$

4.3 Measurement Update

The second step is the "measurement update," where the residuals between the model calculated value $\boldsymbol{h}$ and the measurement date $\boldsymbol{z}$ and added to obtain the updated state, $\boldsymbol{X}_{i+1}$, and the covariance matrix, $\boldsymbol{P}_{i+1}$. at the measurement time. And the measurement data includes both the sum combination and the subtraction combination, $\boldsymbol{z}=[z_{com}\ z_{sub}]^{\mathrm{T}}$. The measurement update is as follows:

$$\begin{aligned} \boldsymbol{K}_{i+1} &= \boldsymbol{P}_{i+1|i}\boldsymbol{H}_{i+1}^{\mathrm{T}}\left(\boldsymbol{R}_{i+1}+\boldsymbol{H}_{i+1}\boldsymbol{P}_{i+1|i}\boldsymbol{H}_{i+1}^{\mathrm{T}}\right)^{-1} \\ \boldsymbol{X}_{i+1} &= \boldsymbol{X}_{i+1|i}+\boldsymbol{K}_{i+1}\left(\boldsymbol{z}_{i+1}-h\left(\boldsymbol{X}_{i+1|i}\right)\right) \\ \boldsymbol{P}_{i+1} &= \left(\boldsymbol{I}-\boldsymbol{K}_{i+1}\boldsymbol{H}_{i+1}\right)\boldsymbol{P}_{i+1|i}\left(\boldsymbol{I}-\boldsymbol{K}_{i+1}\boldsymbol{H}_{i+1}\right)^{\mathrm{T}}+\boldsymbol{K}_{i+1}\boldsymbol{R}_{i+1}\boldsymbol{K}_{i+1}^{\mathrm{T}} \end{aligned} \tag{18}$$

where $\boldsymbol{K}_{i+1}$ is the Kalman gain and $\boldsymbol{R}_{i+1}$ is the measurement noise covariance matrix. This method of updating the covariance matrix preserves its symmetry. The design matrix, $\boldsymbol{H}_{i+1}$, contains linearized partial derivatives of the measurement with respect to each estimated parameter, and is given by the following:

$$\boldsymbol{H}_{i+1}=\begin{bmatrix} \boldsymbol{H}_{\boldsymbol{Y}} & \boldsymbol{H}_{\boldsymbol{T}} & \boldsymbol{0}_{2\times2} & \boldsymbol{0}_{2\times1} \end{bmatrix} \tag{19}$$

And partial derivatives of the measurement with respect to the orbit states, $\boldsymbol{H}_{\boldsymbol{Y}}$, and clock coefficients $\boldsymbol{H}_{\boldsymbol{T}}$ are computed by:

$$\boldsymbol{H}_{\boldsymbol{Y}}=\begin{bmatrix}\dfrac{\partial\rho(t_i)}{\partial\boldsymbol{r}_D(t_i)} & \dfrac{\partial\rho(t_i)}{\partial\boldsymbol{v}_D(t_i)} & \dfrac{\partial\rho(t_i)}{\partial\boldsymbol{r}_L(t_i)} & \dfrac{\partial\rho(t_i)}{\partial\boldsymbol{v}_L(t_i)}\\ \boldsymbol{0}_{1\times3} & \boldsymbol{0}_{1\times3} & \boldsymbol{0}_{1\times3} & \boldsymbol{0}_{1\times3}\end{bmatrix} \tag{20}$$

$$\boldsymbol{H}_{\boldsymbol{T}}=\begin{bmatrix}0 & 0 & 0\\ 1 & \dfrac{\partial z_{\mathrm{sub}}(t_i)}{\partial(c\delta\mathrm{A}_1(t_i))} & \dfrac{\partial z_{\mathrm{sub}}(t_i)}{\partial(c\delta\mathrm{A}_2(t_i))}\end{bmatrix}$$

The elements in the equation are computed from(7)-(10).

5. Navigation Simulation

In this character, attention is paid to determining an appropriate observation setting. Firstly, this paper introduces the chosen satellite orbits. And then this paper analyzes the inter-satellite link, including the observability between two satellites and the converged speed during navigation. Thirdly, this paper analyzes the dynamic characters of two satellites, and the divergence of error over time is studied. At last, an appropriate observation time setting is determined.

5.1 Satellite Orbit

The reference orbit is generated by numerical calculation, and the change of inter-satellite distance is analyzed. The simulation start time and the simulation time duration are set to be January 1, 2023, 00:00:00.00 (UTC), and 40 days. The initial orbital states of the DRO and the LEO expressed in J2000 are listed in Tab. 3, and the force model parameters are listed in Tab. 4.

Table 3. Initial states of the DRO and LEO are expressed in J2000.

Parameters	DRO	Parameters	LEO
x /km	379402.407813576	Semi-major /km	6878.137
y /km	137717.883232907	Eccentricity	0
z/km	45812.450121699	Inclination /°	97.4065
vx/(km/s)	-0.590307515394	Arg. of Perigee /°	0
vy /(km/s)	0.683534139420	RAAN /°	10.3886
vz /(km/s)	0.345590985786	True Anomaly /°	0
Orbit period	13.5 days	Orbit period	1.5 hour

Table 4. Dynamic model and integrator parameters

Parameters	Value
Planetary ephemeris	DE405
Earth gravity	70×70 GGM01C
Lunar gravity	20×20 GL0120B
Sun gravity	Point mass
SRP Radiation pressure coefficient C_R	1.3

Area-mass-ratio (m^2/kg)	0.002
Atmospheric drag coefficient C_D	2.5
Integrator	ABM
Step size/s	60.0

Figure 6 illustrates the time histories of the ranges between the DRO and LEO. Due to the short orbital period of LEO, the periodic change of SST amplitude is very fast, which makes the ranges have more dynamic variation. As shown in the local enlarged figure, due to the long orbital period of the DRO, the amplitude of change is large. As shown in Fig. 6, the SST sequence also has a long period and large amplitude oscillation of about 15 days. In general, if the amplitude of SST is large and the period changes quickly, the measurement configuration is well.

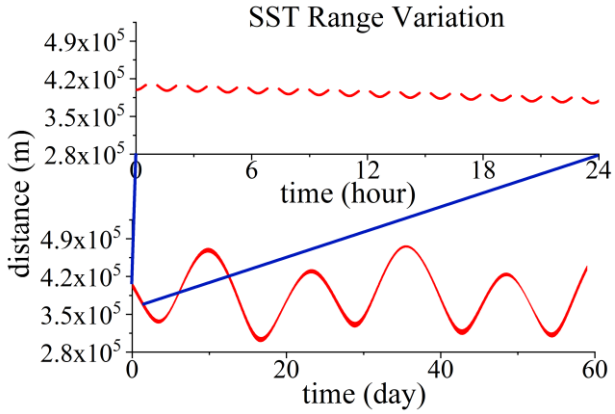

Figure 6. SST Range variation of LEO-DRO

5.2 Analysis of inter-satellite links

K-band is used in this mission, which has a wide beam and high power. And the attitude of the satellite will be corrected to ensure that the antennas of the two satellites are pointing properly, so the only factor affecting. And the accessibility of the inter-satellite link is the shielding of the Earth and the Moon in the cislunar space.

the DRO is visible for 1 hour and invisible for half an hour in one LEO Orbit cycle (1.5 hours) unless it is located outside the special arc segment. To ensure that there is observation data in each observation link, each observation arc segment shall be longer than 0.5 hours. To further determine the appropriate observation radian, the convergence of autonomous navigation is studied by using the lower limit of Cramero.

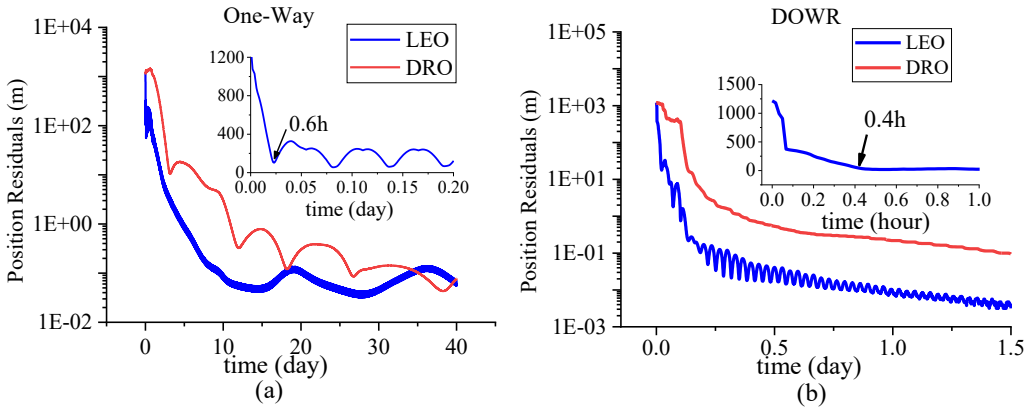

Figure 7. Schematic diagram of orbit error propagation

Figure 7 (a) and (b) respectively show the results of the convergence of the lower limit of Cramero from 1000m and 0.1m/s when the crosslink has continuous observation data under the one-way ranging mode and dual one-way ranging mode. In addition, it can be seen from the two figures that among the two measurement types, the convergence speed of LEO is faster in the first 0.6h. To ensure convergence efficiency, the continuous observation time should be set to more than 0.6h, and 1 hour can be an optional choice.

5.3 Analysis of Orbit Error Propagation

This section establishes a high-accuracy dynamic model, and attention is paid to evaluating the factors which influenced orbit state propagation such as propagation time and initial orbit error. The results can be supportive to determine the duration of the observation break. The orbit error propagation is shown in Fig. 8. The propagation of orbit error can be described by the state transition matrix. As it is shown in Fig. 8, The propagation of orbit error is determined by the state transition matrix of true trajectory, $\mathbf{\Phi}(t_f, t_0)$. Given in the initial time t_0, the state error is δx_0 a Gaussian white noise vector whose mean value is zero, $P(t_0)$ denotes the covariance matrix, so at the time of t_f, the covariance matrix can be calculated by $\mathbf{P}(t_f) = \mathbf{\Phi}(t_f, t_0)\mathbf{P}(t_0)\mathbf{\Phi}^T(t_f, t_0)$. The covariance matrix can be used to analyze the propagation of error.

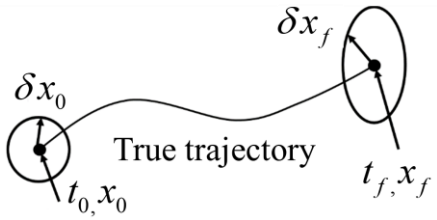

Figure 8. Schematic diagram of orbit error propagation

In the previous study, the navigation accuracy of LEO can be reached at 10 m and 1cm/s, and the navigation accuracy of DRO can be reached at 30m and 0.1mm/s. In this section, these coarse values are used as the initial values for the simulation, and the initial error of Cd and Cr is 10%. Two other different initial orbit errors were used to evaluate the influence of initial error, which is presented in Tab. 5, where three directions have the same value.

Table 5. Initial orbit error for propagations

Initial error	Position (x/y/z (m))		Velocity (x/y/z (m/s))	
	A	B	A	B
LEO	4	100	4E-3	4E-2
DRO	15	100	5E-5	0.01

The result of orbit error propagation of LEO and DRO are shown in Fig. 9. The subgraphs (a), and (b) in the figure correspond to the initial state Settings in models A, and B in Tab. 5 respectively. The left subgraph shows the propagation of position error, the right one shows the propagation of velocity error.

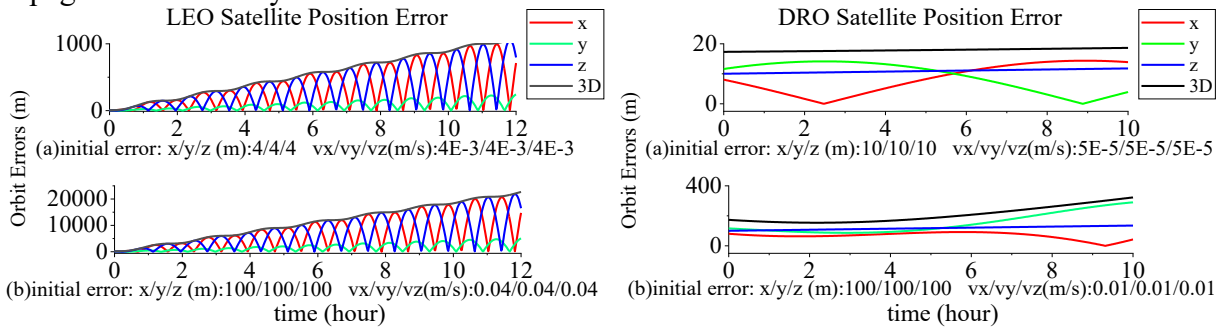

Figure 9. Results of LEO and DRO error propagation analysis

The error propagation results show that with a small input error of LEO, the error will diverge to the level of a kilometer within 11 hours, and the divergence speed is nearly linear with diverge time. The divergence speed of DRO is significantly slower with a small input error than that of LEO. Error divergence of DRO is also linear with divergence time. The larger the error is in the initial state, the faster the error diverges.

The law of error propagation can be supportive for setting the observation break of an inter-satellite link. Since the divergence speed of LEO orbit error is faster than that of DRO, the error divergence of LEO will be mainly considered when setting the observation break of the inter-satellite link between LEO and DRO. Because LEO can rapidly diverge to the KM level within 11 hours, the observation interval should not be longer than 11h.

At the same time, considering the influence of signals blocked by Earth and Moon and the convergence time of navigation, the optimal continuous observation time is about an hour. Under the condition of ensuring the convergence efficiency and quality of navigation, flight costs should be considered to improve the service life as much as possible. **The inter-satellite observation period is 12 hours, which has 1 hour for observation and 11 hours for observation break**.

5.4 Simulation Results

A previous study [7] showed that position and velocity uncertainties of 1km and 0.1m/s, respectively, can be achieved in deep space using optical measurements. In this paper, during the autonomous navigation, parameters including the position and velocity of satellites, the absolute clock of DRO, the equipment delays in the satellite link, the solar radiation pressure parameter, and the atmospheric drag parameter are estimated. In this section, attention is paid to evaluating the navigation performance influenced by various factors, the EKF is used to process instantaneous range measurements of different scenarios subjected to different dynamic models, integrator models, and measurement types. Firstly, in the DOWR system, this paper uses

different integrators to evaluate the influence of integrator and integrator steps, and then different accuracy of dynamic models are chosen to evaluate the influence of dynamic error. Secondly, in the One-Way Ranging system, and two types of measurement alternatives, we evaluated the influence of measurement type. Statistical analysis was conducted on the total results. The time series of the 3D position, the 3D velocity, and the absolute clock onboard DRO between true trajectories and estimated trajectories over time were computed. We then counted the 3D RMS values of the last 8 days of data, the different scenarios were processed one by one

5.4.1 Dual One-Way Ranging System

(1) Different Types of Integrators

Considering the satellite's limited computing power, we use the RK4 and RKF78 integrators to evaluate the influence of integrators. In this paper, the simulation of using the RK4 integrator is marked as Simulation. 1 or Simu. 1 for short, similarly, simulation of RKF 78 integrator is marked as Simulation. 2 or Simu. 2.

The Ephemeris and the parameters of the dynamic and integrator model are presented in Tab. 6.

Table 6. Ephemeris and the parameters of dynamic and integrator model

Parameters	Value
Planetary ephemeris	JPL DE405
Earth gravity	50×50 GGM01C
Lunar gravity	15×15 GL0120B
Sun gravity	Point mass
SRP Radiation pressure coefficient C_R	μ=1.3, σ=0.1
Atmospheric drag C_D	μ=2.5, σ=0.1
Area-mass-ratio	0.002 m^2/kg
Integrator	RK4/RKF78
Step size	60 s

The filter parameters of different integrators are presented in Tab. 7. Only when an appropriate noise process was selected, the covariance matrix can get the navigation accuracy correctly. The RKF78 integrator has high order, which can get higher accuracy of dynamic propagation, so the smaller process noise is set in the simulation.

Table 7. Filter parameters

	Process Noise(m/s^2)	
number	Simu. 1	Simu. 2
Integrator	RK4	RKF78
DRO(R/T/N)	$10^{-8}/10^{-8}/10^{-8}$	$10^{-9}/10^{-9}/10^{-9}$
LEO(R/T/N)	$10^{-6}/10^{-6}/10^{-6}$	$10^{-7}/10^{-7}/10^{-7}$

The navigation result of using RK4 and RKF78 integrator is shown in Fig. 10-12. In Fig. 10, the subgraph (a) and (c) is the times series of the position accuracy of LEO, and the local zoom is also shown in the subgraphs, and two subgraphs show the convergence of LEO in three directions using different integrators. Similarly, subgraphs (b) and (d) show the information on DRO. In this paper, the convergence time is as the duration time that the accuracy of three directions all converged below 100m, which is also shown in Fig. 10. Figuration 11 shows the accuracy of the clock onboard DRO. The subgraph (a) and (c) show the times series of the

accuracy of clock offset of DRO, and the subgraph (b) and (d) show that of clock drift offset of DRO. The SRP accuracy of DRO and atmospheric drag parameters of LEO is shown in Fig. 12.

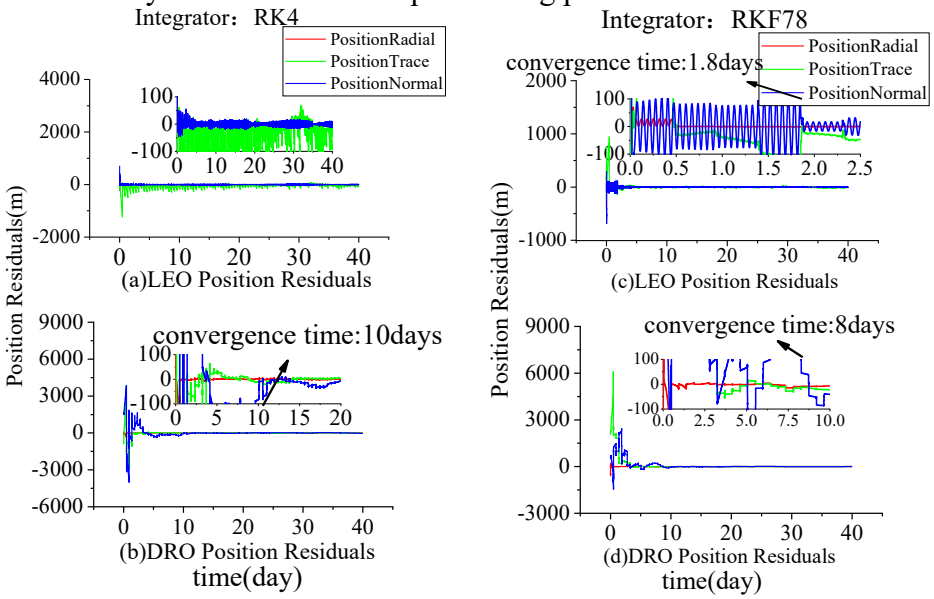

Figure 10. Time series of positioning residuals of LEO and DRO.

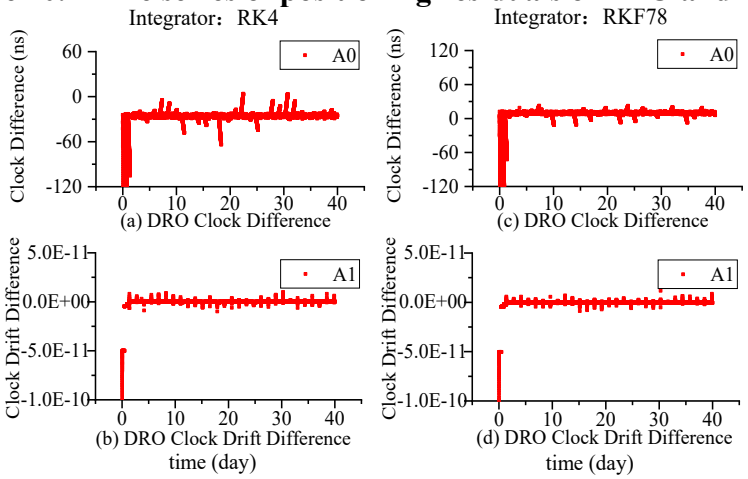

Figure 11. Time series of residuals of clock difference and clock drift difference of clock onboard DRO

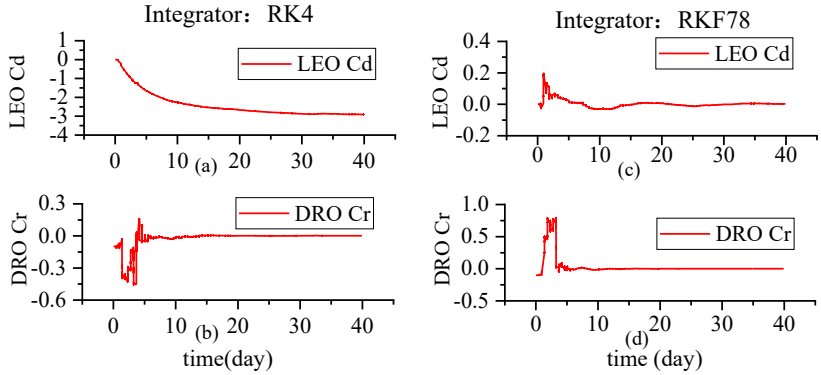

Figure 12. Time series of atmospheric drag parameters' residuals of LEO and SRP residuals of DRO.

Figuration 12 shows that a low-order integrator can damage the estimation of Cd, which indirectly affects the dynamic model accuracy of LEO. From Fig. 10 and Fig. 11, we can get the information that the accuracy of the integrator largely affected the accuracy and the converging speed of navigation, and the navigation of LEO is greatly affected by the integrator.

(2) Different integration steps

This section researches the influence of integration steps. Four different accuracy dynamic models are used in navigation, and attention is paid to evaluating the navigation performance in each different integration step. Similarly, the parameters of dynamic models and integrators used in orbit determination are presented in Tab. 8. And the filter parameters are presented in Tab. 9. When the integration step is 60 s, the parameters of the dynamic model and integrator are the same as that of Simu. 2. The same as the research of integrator, the simulations of integration steps which are 30 s, 5min, and 10min are marked as Simu.3-5 in order.

Table 8. Ephemeris and the parameters of dynamic and integrator model

Parameters	Value
Planetary ephemeris	JPL DE405
Earth gravity	50×50 GGM01C
Lunar gravity	15×15 GL0120B
Sun gravity	Point mass
SRP Radiation pressure coefficient C_R	μ=1.3, σ=0.1
Atmospheric drag C_D	μ=2.5, σ=0.1
Area-mass-ratio	0.002 m^2/kg
Integrator	RKF78
Step size	30 s/60 s/5 min/10 min

The smaller integration steps can get higher accuracy of dynamic propagation, so the smaller process noise is set in the simulation.

Table 9. Filter parameters

	Process Noise(m/s^2)			
number	Simu. 3	Simu. 2	Simu. 4	Simu. 5
Integration step	30 s	60 s	5 min	10 min
DRO(R/T/N)	$10^{-9}/10^{-9}/10^{-9}$	$10^{-9}/10^{-9}/10^{-9}$	$10^{-8}/10^{-8}/10^{-8}$	$10^{-8}/10^{-8}/10^{-8}$
LEO(R/T/N)	$10^{-7}/10^{-7}/10^{-7}$	$10^{-7}/10^{-7}/10^{-7}$	$10^{-7}/10^{-7}/10^{-7}$	$10^{-6}/10^{-6}/10^{-6}$

The Same as above, the results of integration steps are shown in Fig13-15, the result of Simu. 2 is shown in Fig. 10-12 already.

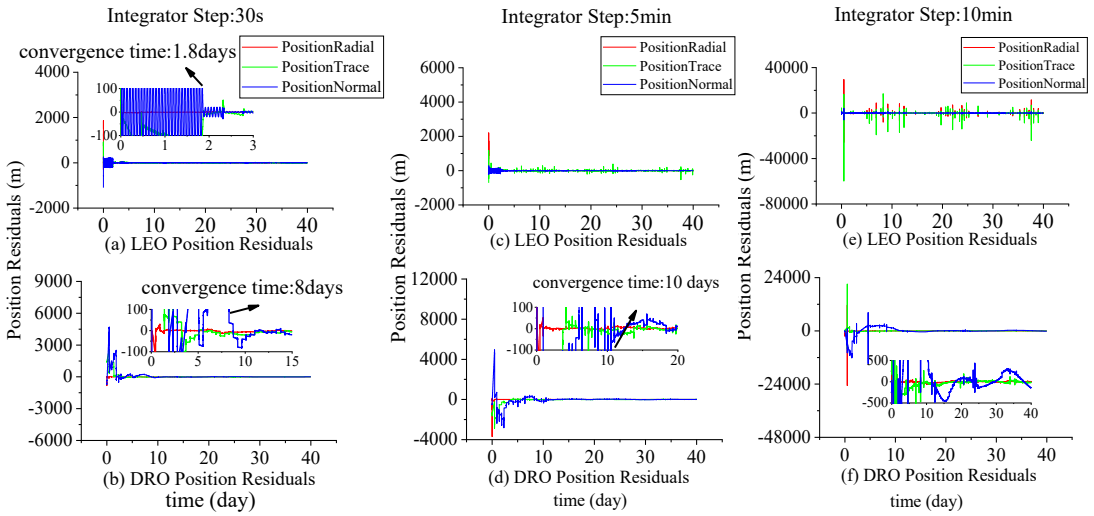

Figure 13. Time series of position accuracy of LEO and DRO integrator.

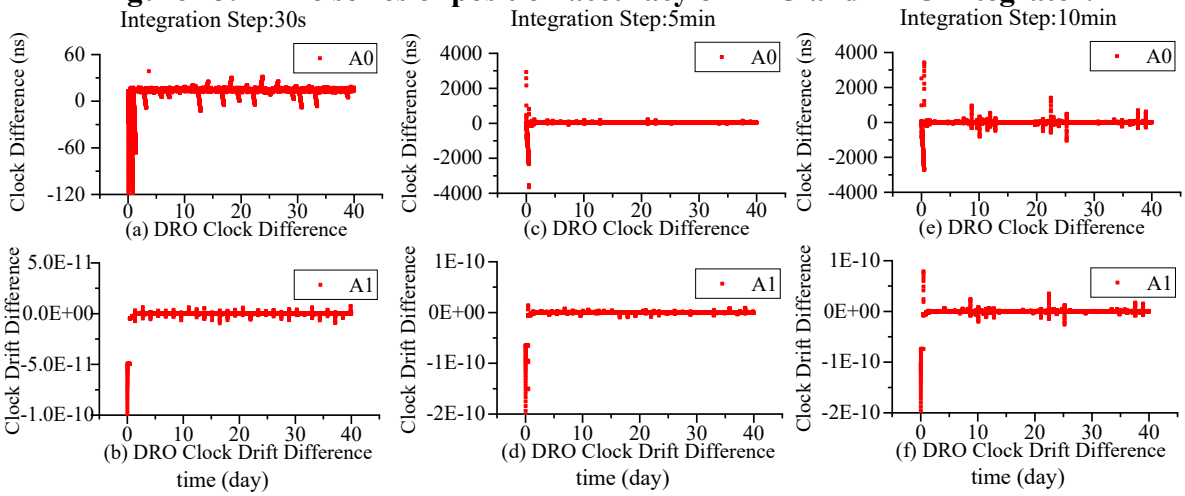

Figure 14. Time series of residuals of clock difference and clock drift difference of clock onboard DRO

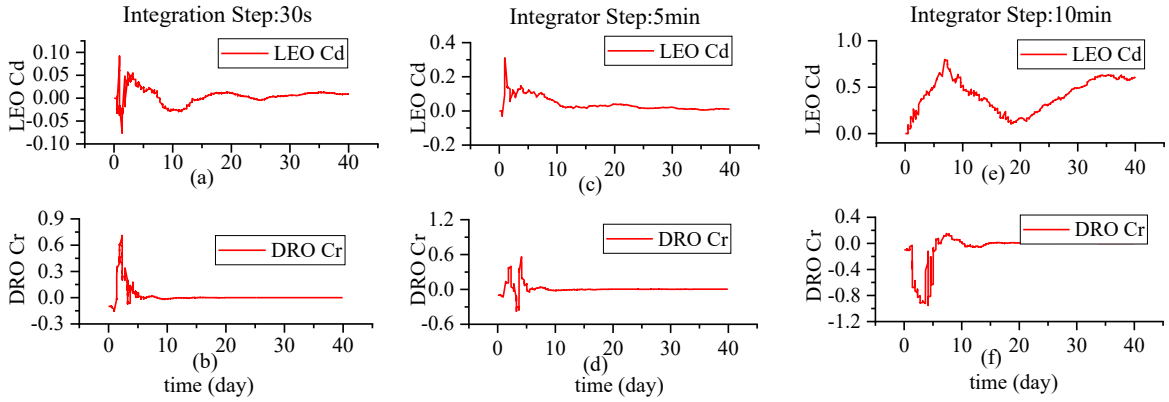

Figure 15. Time series of atmospheric drag parameters residuals of LEO and SRP residuals of DRO.

Figuration .15 and Fig. 12 show that the atmospheric drag parameters can't be converged when the integration step is 10min, and longer integration steps cause larger divergence in the earlier stage. but the SRP parameters are less affected by the integration steps. Figuration 13 and Fig. 10 show that when the integration step is short than 60 s, the position accuracy in each direction of

LEO can converge to 100m in a very short time, but when the integration time is longer than 5min, they cannot converge to 100m. DRO isn't very sensitive to integration steps, only when the integration steps are longer than 10min, position accuracy can't converge to 100m. The divergency of position accuracy in the earlier stage is largely affected by this factor. However, the clock accuracy is not very sensitive to it, which is shown in Fig. 11 and Fig. 15. The results show that the navigation of LEO is greatly affected by integration steps.

(3) Different dynamic models

This section researches the influence of dynamic accuracy. Three different accuracy dynamic models are used in navigation, and attention is paid to evaluating the navigation performance in each model. Similarly, the parameters of dynamic models and integrators used in orbit determination are presented in Tab. 10. And the different filter parameters are presented in Tab. 11. And each simulation is marked as Simu.6-7 in order.

Table 10. Filter parameters

Parameters	Model-A	Model-B	Model-C
Planetary ephemeris	JPL DE405	JPL DE405	JPL DE405
Earth gravity	70×70 GGM01C	50×50 GGM01C	30×30 GGM01C
Lunar gravity	20×20 GL0120B	15×15 GL0120B	10×10 GL0120B
Sun gravity	Point mass	Point mass	Point mass
SRP Radiation pressure coefficient C_R	μ=1.3	μ=1.3, σ=0.1	μ=1.3, σ=0.1
Atmospheric drag C_D	μ=2.5	μ=2.5, σ=0.1	μ=2.5, σ=0.1
Area-mass-ratio	0.002 m^2/kg	0.002 m^2/kg	0.002 m^2/kg
Integrator	RKF78	RKF78	RKF78
Step size	60 s	60 s	60 s

Higher accuracy of dynamic propagation needs the smaller process noise in the simulation.

Table 11. Filter parameters

	Process Noise(m/s^2)		
number	Simu. 6	Simu. 2	Simu. 7
Dynamic Model	Model-A	Model-B	Model-C
DRO(R/T/N)	$10^{-10}/10^{-10}/10^{-10}$	$10^{-9}/10^{-9}/10^{-9}$	$10^{-7}/10^{-7}/10^{-7}$
LEO(R/T/N)	$10^{-8}/10^{-8}/10^{-8}$	$10^{-7}/10^{-7}/10^{-7}$	$10^{-5}/10^{-6}/10^{-5}$

The Same as above, the results of integration steps are shown in Fig14-16, the results of dynamic model-B were presented in Fig 16-18.

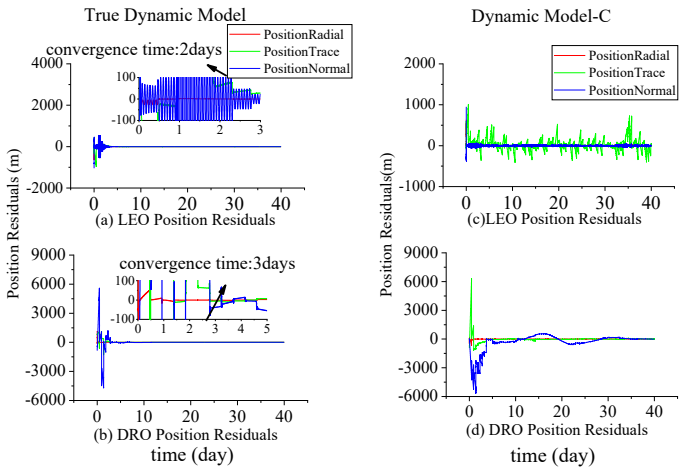

Figure 16. Time series of positioning residuals of LEO and DRO.

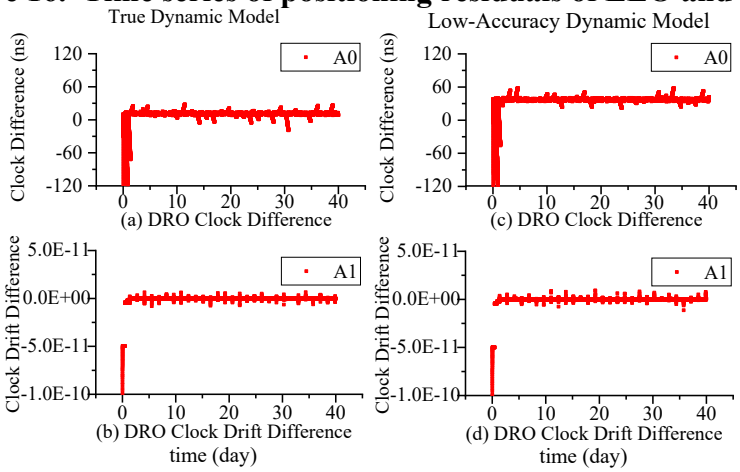

Figure 17. Time series of residuals of clock difference and clock drift difference of clock onboard DRO

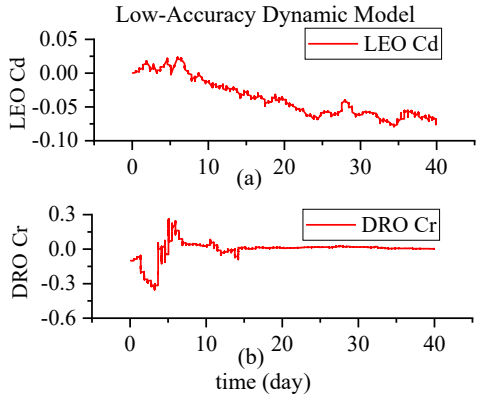

Figure 18. Time series of residuals of atmospheric drag parameters of LEO and SRP of DRO

Figuration 16 shows that both the position accuracy of LEO and DRO get converged in a short time using the high-accuracy dynamic model, Fig. 16 shows LEO get converged needs the time duration of 1.8 days, and DRO needs 8 days using a middle-accuracy dynamic model, while they can't converge to 100m using a low-accuracy dynamic model. The divergency of position accuracy in the earlier stage is affected by this factor. However, the clock accuracy is not sensitive to it, which can be shown in Fig. 11 and Fig. 14. Figuration 18 shows that the

atmospheric drag parameters of LEO cannot converge, but the SRP of DRO converges well. The results show that the navigation of LEO is greatly affected by the dynamic model.

5.4.2 One-Way Ranging System And DOWR + One-Way

The Dynamic model and integrator used in the one-way ranging system and the alternate system are the same as Model-B which is presented in Tab. 12. And the filter parameters are presented in Tab. 10. Similarly, simulations are numbered as Simu. 8 and Simu. 9.

Table 12. Filter parameters

	Process Noise(m/s^2)	
Number	Simu. 8	Simu. 9
Measurement Type	One-Way	DOWR + One-Way
DRO(R/T/N)	$10^{-9}/10^{-9}/10^{-9}$	$10^{-9}/10^{-9}/10^{-9}$
LEO(R/T/N)	$10^{-7}/10^{-7}/10^{-7}$	$10^{-7}/10^{-7}/10^{-7}$

The results are shown in Fig. 20-22:

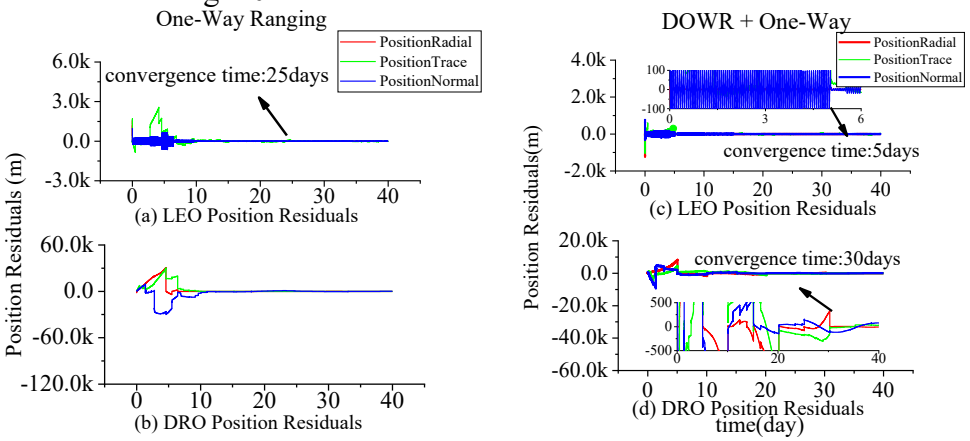

Figure 19. Time series of positioning residuals of LEO and DRO.

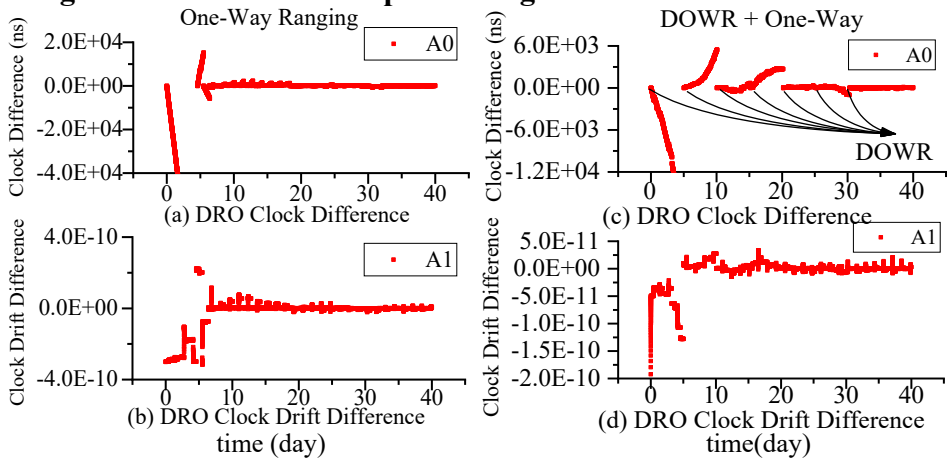

Figure 20. Time series of residuals of clock difference and clock drift difference of clock onboard DRO

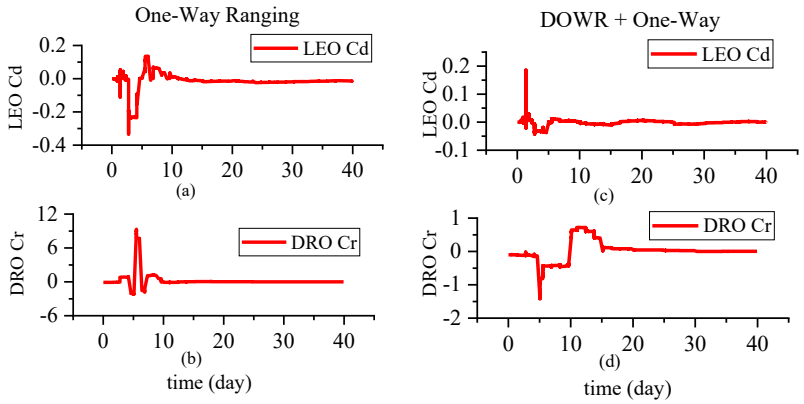

Figure 21. Time series of atmospheric drag parameters' residuals of LEO and SRP residuals of DRO.

Figuration 19 shows that, in the one-way ranging system, the position accuracy diverged to 3 km in the earlier stage, and it can converge to 100 m in 25 days, while that of DRO diverged to 30 km in the earlier stage and it can't converge to 100 m in 40days. And results of the DOWR + One-Way ranging system are much better. The position accuracy diverged of LEO and DRO in the earlier stage are about 1km and 10km, and the convergence time of LEO and DRO are 5 days and 30 days.

The subgraph (a) and (b) in Fig. 20 show the accuracy of clock offset and clock drift difference of DRO using the one-way ranging system. and clock offset and clock drift difference oscillate violently as they converge, but they can converge to a high-level accuracy relatively at last. The subgraph (c) and (d) in Fig. 20 show that using the alternate measurement mode. Compared with only using one-way ranging measurement data, they diverge slowly, and the accuracy of clock offset can converge to a very high level as soon as the system gets DOWR measurement data, then the result will diverge. After some time, they can converge to a very high level. When the DOWR system is used, the accuracy and convergence speed of the clock can be greatly improved.

Results show that DRO and converge speed are sensitive to measurement type.

5.4.3 Discussion

Table 13 shows the 3D RMS values of position accuracy, velocity accuracy, clock accuracy, and the convergence time of DRO and LEO in the last 8 days. In this paper, the convergence time is as the duration time that the accuracy of three directions all converged below 100m.

Table 13. 3D RMS accuracy of the position, and velocity, for the DRO-LEO scenario

Number	Measurement Mode	Dynamic Model	Integrator	Step	Satellite	Position Accuracy (m)	Velocity Accuracy (m/s)	Clock Accuracy (ns)	Convergence time (days)
Simu. 1	DOWR	High accuracy	**RK4**	60 s	DRO	21.65	1.14E-04	24.85	10
					LEO	51.02	5.70E-02		-
Simu. 2	DOWR	High accuracy	**RKF78**	60 s	DRO	6.37	1.39E-05	10.10	8
					LEO	8.65	9.62E-03		1.8
Simu. 3	DOWR	High accuracy	RKF78	**30 s**	DRO	5.54	1.37E-05	14.81	8
					LEO	8.92	9.95E-03		1.8

Simu. 4	DOWR	High accuracy	RKF78	**5 min**	DRO	8.02	2.95E-05	39.31	10
					LEO	23.36	2.60E-02		-
Simu. 5	DOWR	High accuracy	RKF78	**10 min**	DRO	185.76	6.92E-04	22.49	-
					LEO	742.32	8.27E-01		-
Simu. 6	DOWR	**True model**	RKF78	60 s	DRO	0.51	1.86E-06	12.20	3
					LEO	0.57	1.88E-03		2
Simu. 7	DOWR	**Low accuracy**	RKF78	60 s	DRO	68.94	1.68E-04	37.62	-
					LEO	200.90	2.25E-01		-
Simu. 8	**One-Way**	High accuracy	RKF78	60 s	DRO	120.38	4.88E-04	86.44	-
					LEO	22.36	2.50E-02		25
Simu. 9	**DOWR + One-Way**	High accuracy	RKF78	60 s	DRO	73.34	2.96E-04	46.62	30
					LEO	22.56	2.52E-02		5

Due to the short orbit period, the convergence time of LEO is shorter than that of DRO in most scenarios. And the simulations have obtained high precision time synchronization results, which can get the accuracy of time converged below 100ns. Using a high-accuracy dynamic model, the position accuracies of DRO and LEO are about 0.5 m, which is equal to thermal noise. The difference in integrator models caused different navigation results, and LEO is largely affected, and the measurement type greatly influences the converge speed and the accuracy of the clock.
It's obvious that the higher the order of the integrator, the shorter the integration step, and the higher accuracy of the dynamic model can get the better the navigation performance. In terms of navigation performance, the result of Simu. 2, Simu. 3 and Simu. 6 can meet the engineering needs. However, considering the power consumption of the K-band payload, the navigation model configuration of Simu 2 is the most ideal option.

6. Conclusions

This paper mainly focuses on evaluating the navigation performance of the inter-satellite link between LEO and DRO. These conclusions can be supportive for engineering work by establishing a high-fidelity measurement model and analyzing systematically, they are as follow:

(1) Considering the satellites' dynamic characters and an inter-satellite link. By using the DOWR system, the DRO and LEO can get a position accuracy of 10m and get a clock accuracy of about 10ns. Two satellites can get converged in a few days by establishing an appropriate observation model and reliable dynamical integration model.

(2) The navigation performance influenced by factors such as integrators, integration steps, and the accuracy of the dynamic model is analyzed. These three types of simulations have relationships with the dynamic integrations, and it is obvious that LEO is very sensitive to the accuracy of dynamic integrations. Considering the short LEO period, the integration step should not be too long. and the modeling accuracy of the dynamic should be ensured. According to these analyses and results, a high-order integrator like RKF78, a relatively short integration step like the 60s, and a relatively high-accuracy dynamic model like the Model-B which is represented in Tab. 10 can be good options for navigation.

(3) This paper also evaluates the influence of different measurement types. Results show that the accuracy of DRO and the convergence time of the orbit determination process is sensitive to the measurement type. The combination measurement mode of one-way ranging and DOWR can improve the convergence speed by taking advantage of DOWR. and it can reduce the resource cost simultaneously. However, the position accuracy of DRO is not as good as using the DOWR system.

9. References

[1] WANG A. ZHANG C. WANG s, et al. “Design Considerations for Access in to Earth-Moon DROs With Lunar Free-return Trajectory”. Manned Spaceflight, Vol. 28, No. 1, pp. 81-89, 2022.

[2] Zeng H, Li z, Peng k, et al. “Research on Application of Earth-Moon NRHO and DRO for Lunar Exploration.” Journal of Astronautics, Vol. 41, No. 7, pp. 910-919, 2020.

[3] Thompson, Michael R. Forsman, et al. “Cislunar Navigation Technology Demonstrations on the CAPSTONE Mission.” Proceedings of the 2022 International Technical Meeting of The Institute of Navigation, Long Beach, California, January 2022, pp. 471-484.

[4] Wang W, Shu L, Liu J, et al. “Joint navigation performance of distant retrograde orbits and cislunar orbits via LiAISON considering dynamic and clock model errors.” Navigation, Vol. 66, No. 4, pp. 781-802, 2019.

[5] Christopher, H. and K. Elliott. “Understanding GPS Principles and Applications, Second Edition.” 2005: Artech. 1.

[6] R Kroes. “Precise relative positioning of formation flying Spacecraft using GPS.” Delft University of Technology, 2006.

[7] Ma X, Fang J, Ning X, et al. “Autonomous celestial navigation for a deep space probe approaching a target planet based on ephemeris correction.” Proceedings of the Institution of Mechanical Engineers, Part G: Journal of Aerospace Engineering. Vol. 229, No. 14, pp. 2681-2699, 2015.

ACKNOWLEDGEMENTS

This work was supported by the Strategic Priority Research Program of the Chinese Academy of Sciences, Grant No. XDA30010000. The authors wish to thank Shi Yu for his beneficial comments on this paper.